


Charge-Induced Artifacts in Nonlocal Spin-Transport Measurements: How to Prevent Spurious Voltage Signals

Frank Volmer^{1,2}, Timo Bisswanger¹, Anne Schmidt¹, Christoph Stampfer^{1,3} and Bernd Beschoten^{1,*}

¹*2nd Institute of Physics and JARA-FIT, RWTH Aachen University, Aachen 52074, Germany*

²*AMO GmbH, Advanced Microelectronic Center Aachen (AMICA), Aachen 52074, Germany*

³*Peter Grünberg Institute (PGI-9), Forschungszentrum Jülich, Jülich 52425, Germany*

 (Received 6 December 2021; revised 17 May 2022; accepted 20 May 2022; published 13 July 2022)

To conduct spin-sensitive transport measurements, a nonlocal device geometry is often used to avoid spurious voltages that are caused by the flow of charges. However, in the vast majority of reported nonlocal spin-valve, Hanle spin precession or spin Hall measurements, background signals have been observed that are not related to spins. We discuss seven different types of these charge-induced signals and explain how these artifacts can result in erroneous or misleading conclusions when falsely attributed to spin transport. The charge-driven signals can be divided into two groups: signals that are inherent to the device structure and/or the measurement setup and signals that depend on a common-mode voltage. We designed and built a voltage-controlled current source that significantly diminishes all spurious voltage signals of the latter group in both dc and ac measurements by creating a virtual ground within the nonlocal detection circuit. This is especially important for lock-in-based measurement techniques, where a common-mode voltage can create a phase-shifted, frequency-dependent signal with an amplitude several orders of magnitude larger than the actual spin signal. Measurements performed on graphene-based nonlocal spin-valve devices demonstrate how all spurious voltage signals that are caused by a common-mode voltage can be completely suppressed by such a current source.

DOI: [10.1103/PhysRevApplied.18.014028](https://doi.org/10.1103/PhysRevApplied.18.014028)

Two of the most commonly used device geometries for spin-transport measurements are nonlocal spin-valve and nonlocal Hall bar geometries [1–8]. In such devices there is no spatial overlap between the injection circuit over which a charge current is driven [circuit with electrodes I_+ and I_- in Fig. 1(a)] and the detection circuit in which the spin signal is nonlocally probed [circuit with electrodes V_+ and V_- in Fig. 1(a)]. This device scheme is argued to prevent spurious voltage signals because of a putative avoidance of any charge flow in the nonlocal detection circuit [1–4]. In real devices, however, there are several mechanisms that can lead to a flow of charges in the nonlocal part of the device. In this article we discuss seven different mechanisms that can result in charge-induced nonlocal voltages. All of the discussed mechanisms are of such a fundamental nature that they can occur in any material system.

In this context, it is important to emphasize that our discussion is not exhaustive as we explicitly do not include material-specific phenomena that can lead to nonlocal voltage signals. One prominent example is the occurrence

of large nonlocal signals either at the charge neutrality point in graphene or by opening a band gap in bilayer graphene. Although these nonlocal signals have been attributed to topological currents or the valley Hall effect [9–12], more recent studies rather explain these measurements by generic, nontopological edge currents that lead to a flow of charges in the nonlocal part of the device [13–15]. The ensuing debate about the actual underlying physics [15–17] follows other controversial discussions such as those about the correct interpretation of nonlocal spin Hall effect measurements or spin-transport measurements in topological insulators. For the latter two cases, several studies already demonstrated the occurrence of charge-induced nonlocal voltages that might have been falsely attributed to spin-related effects in preceding publications [18–23]. This highlights the importance for a comprehensive review of the mechanisms that can create spurious voltage signals, which is one essential part of this article. Besides already known sources of charge-induced nonlocal voltages, we also discuss a spurious voltage signal that depends on the common-mode voltage in the nonlocal part of the device and that has not been considered so far. The amplitude of this signal scales with the applied measurement frequency. At higher frequencies

*bernd.beschoten@physik.rwth-aachen.de

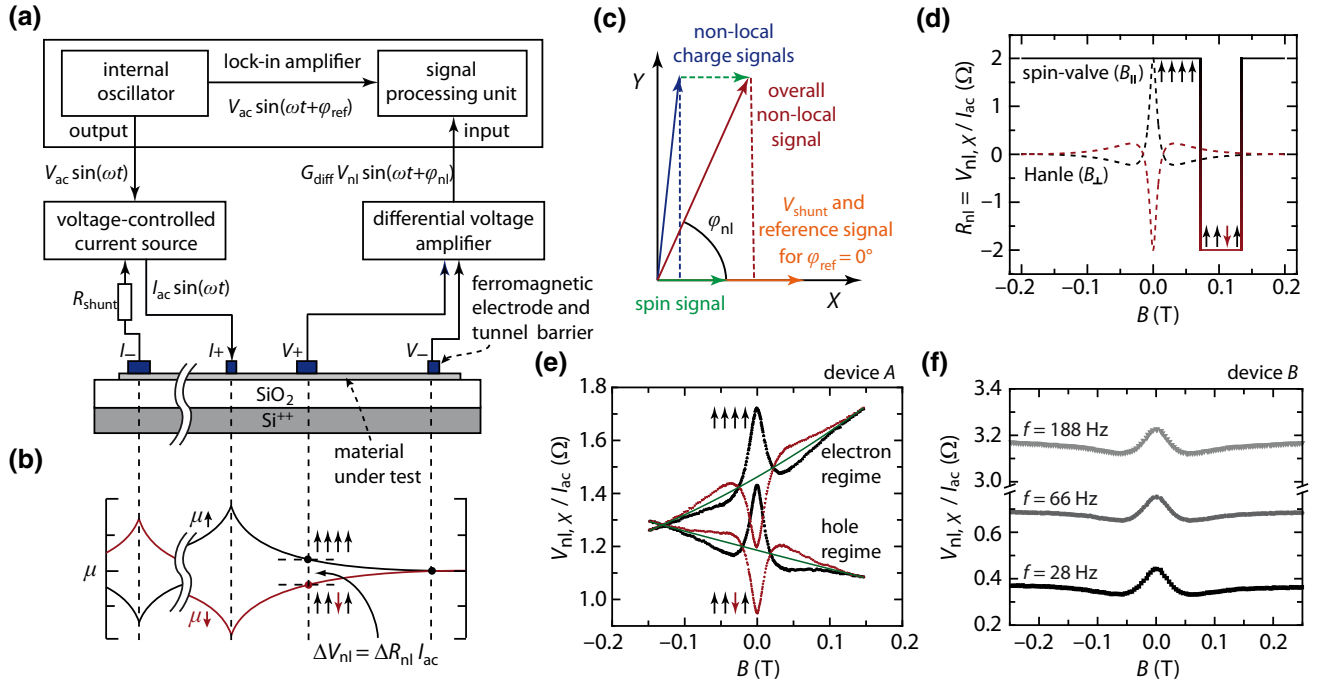


FIG. 1. (a) Lock-in-based, nonlocal measurement scheme of a lateral spin-valve device. A charge current gets spin polarized by flowing through the ferromagnetic electrodes I_+ and I_- and, therefore, creates the quasi-chemical potentials depicted in panel (b) for majority and minority spins. (c) As the spin signal is directly linked to the current in the injection circuit, both signals should be in phase with each other (the latter can be measured, for example, over a shunt resistor). As long as the voltage-to-current converter is driving the current in phase to the applied reference voltage from the lock-in, the spin signal should appear only in the X channel of the lock-in. In real measurements charge-induced signals also appear that can be either in phase or out of phase with the applied current. (d) Without these spurious signals, both spin-valve (solid line) and Hanle spin precession (dashed lines) measurements should be symmetric around $R_{nl} = 0$. Instead, in experiments a background signal is almost always measured that changes, e.g., by going from the electron into the hole regime (e) or by merely increasing the measurement frequency (f).

this spurious voltage signal will mask any spin signal, which is the likely reason why the vast majority of reported nonlocal spin-valve, Hanle spin precession, and spin Hall measurements were conducted with either dc currents or ac currents at very low frequencies (≤ 30 Hz) [24–40]. We demonstrate that both this frequency-dependent spurious voltage signal and two others, which are also caused by the common-mode voltage in the detection circuit, can be completely removed by creating a virtual ground within the nonlocal part of the device.

In this article, we first discuss in Sec. I the fundamental principles behind nonlocal spin measurements to lay the basis for the discussion of the charge-induced signals. In Sec. II we explain the mechanisms responsible for the charge-induced signals and (if available) discuss ways how their contribution to a nonlocal measurement can be minimized. In Sec. III we discuss in detail the one charge signal whose amplitude scales with the measurement frequency and demonstrate how this signal can be removed from the measurement by using a current source that we designed and built for this purpose.

I. PRINCIPLES OF A NONLOCAL SPIN TRANSPORT MEASUREMENT

We discuss the mechanisms behind the occurrence of charge-induced, nonlocal voltages using the example of a lateral spin-valve device whose nonlocal signal is measured with a lock-in technique [Fig. 1(a)]. But we note that many of the discussed charge-induced signals also occur in other measurement techniques (including dc measurements) and other device geometries (e.g., Hall bar structures for the nonlocal detection of the spin Hall effect). In our example the sinusoidal voltage signal $V_{ac} \sin(\omega t)$ from the internal oscillator of the lock-in amplifier is used as a reference signal for a voltage-to-current converter. This converter is driving a current $I_{ac} \sin(\omega t)$ through the device under test (DUT) between the two ferromagnetic electrodes in the injection circuit denoted I_+ and I_- . It is assumed that the voltage-to-current converter only creates a negligible phase shift between the reference voltage and the current through the device (probed, e.g., by the voltage drop over a shunt resistor R_{shunt}).

The applied charge current gets spin polarized by the ferromagnetic electrodes and therefore creates a spin accumulation in the material right below the electrodes [1–3]. This is depicted as a quasichemical potential for each spin orientation in Fig. 1(b). Because of the gradient in the spin accumulation, spins also diffuse from the I_+ electrode towards the nonlocal part of the device. The corresponding spin accumulation in this part decreases exponentially because of relaxation processes and can be probed between the spin-sensitive, ferromagnetic electrodes (V_+ and V_-) with a differential voltage amplifier [1–3].

If the DUT has a spin diffusion coefficient D_s , the time that is needed for the spins to diffuse a distance L into the nonlocal region is of the order of L^2/D_s (e.g., for the majority of reported spin-transport experiments in graphene, this time is between 500 ps and 10 ns). In typical measurements this time is several orders of magnitude shorter than the period of the applied ac signal. Therefore, there cannot be any measurable phase that is caused by spin diffusion between the applied ac current, which creates the spin accumulation in the first place, and the measured nonlocal spin signal. Accordingly, any nonlocal signal that has a phase is either due to a measurement artifact or is linked to a physical phenomenon that is not connected to spins. In this respect a lock-in amplifier now becomes important, as it can decompose the overall nonlocal signal in contributions that are in phase and out of phase to its internal oscillator [Fig. 1(c)]. The X channel (sometimes also called Re or Real channel) of the lock-in measures the amplitude of the nonlocal voltage that is in-phase to the internal oscillator, whereas the Y channel (Im or Imag channel) measures the signal that is shifted by 90° . According to the above explanation, the spin signal should be entirely located within the X channel of the lock-in [green arrow in Fig. 1(c)].

In Fig. 1(d) the theoretically expected curves for a spin-valve and a Hanle spin precession measurement are depicted for the case that only the bare spin signal is present in a nonlocal measurement. For the spin-valve measurement, the magnetic field B is applied in plane to the material and antiparallel to the magnetization of the ferromagnetic electrodes. Different widths of the electrodes lead to different coercive fields because of shape anisotropy [41,42]. In Figs. 1(b) and 1(d) it is assumed that electrode V_+ switches first (the four arrows represent the magnetization direction going from electrode I_- to V_-). Therefore, V_+ will no longer probe the spin-up but rather the spin-down potential, which should only lead to a sign reversal of the measured voltage (see the detailed explanations with theoretical derivations in Refs. [1–3]). If the nonlocal resistance R_{nl} is calculated by normalizing the nonlocal voltage by the applied current, the corresponding spin-valve curve should be perfectly centered around $R_{nl} = 0$ [Fig. 1(d)]. If the magnetic field B is applied in the out-of-plane direction, Hanle spin precession curves can be measured both

in the case of a parallel orientation of the respective magnetization directions of the I_+ and V_+ electrodes [black dashed curve in Fig. 1(d)] and the respective antiparallel orientation (red dashed curve). These curves are expected to be mirror images of each other and they should converge to zero at high magnetic fields because of a complete dephasing of the spins [1–3].

Instead, Fig. 1(e) depicts typical experimental Hanle curves with obvious charge-related background signals that are measured in both the hole and the electron regimes of a graphene-based spin-valve device (see the discussion in Sec. IV how the occurrence of these spurious signals may change for other materials and device structures, e.g., metallic spin-valve devices). The background signal can be easily calculated by the arithmetic mean of the two curves for parallel and antiparallel orientation [green curves in Fig. 1(e)] and can be fitted by a second-order polynomial function. Subtracting this background from the measured data results in Hanle curves as depicted in Fig. 1(d), i.e., curves that are perfectly centered around $R_{nl} = 0$ and can be well fitted with models that only consider a spin signal [1–3]. It was shown that this kind of magnetic-field-dependent background signal can be explained by a combination of a current-spreading effect and the Hall effect [19,43], the latter causing the slope to change when tuning the device from the hole into the electron regime.

To highlight the previously described background signal whose amplitude increases towards higher frequencies, we use another graphene-based spin-valve device for the sake of simplicity. For this device, the current spreading effect is minimized by improving the device fabrication process (see the explanation in Sec. II A). As a result, the corresponding Hanle curves in Fig. 1(f) do not have a magnetic-field-dependent background signal. Instead, it is seen how a constant offset voltage increases for increasing frequencies $f = \omega/(2\pi)$ of the applied current. It should be noted that in Fig. 1(f) only the projection of the underlying charge-induced, nonlocal voltage in the X channel is depicted [compare to the blue arrow in Fig. 1(c)]. As explained in the following sections, the underlying charge-induced signal exhibits a phase close to 90° . Accordingly, the signal in the Y channel increases significantly more, even pushing the channel into an overload condition for frequencies higher than 188 Hz in the case of this device, which eventually leads to measurement artifacts of the spin signal in the X channel.

There are a variety of reasons for trying to prevent such charge-induced signals from appearing in nonlocal measurements. The most obvious ones are that such signals can no longer be falsely attributed to spin-related effects and that the analysis of the spin data gets much simpler. Additionally, there is also the benefit to improve the signal-to-noise ratio of the spin measurement via three effects. First, the gain in the differential voltage amplifier and the sensitivity of the lock-in amplifier can be optimized for the

amplitude of the spin signal. Second, preventing a flow of charges in the nonlocal detection circuit will also prevent such currents contributing noise to the measurement. Third, to be able to increase the measurement frequency opens the possibility to probe the spin signal in low-noise frequency bands far away from, e.g., the $1/f$ noise at low frequencies or typical interference frequencies of 50 or 60 Hz.

II. OVERVIEW OF NONLOCAL CHARGE SIGNALS

Besides the actual spin signal V_S , there are at least seven other contributions to the overall nonlocal signal V_{nl} that will be discussed in detail in the following sections:

$$V_{nl} = V_S + (V_{CS} + V_T + V_{IBC} + V_{CI}) + (V_L + V_{CMRR} + V_{CC}). \quad (1)$$

These contributions can be divided into two groups. The first group consists of signals that are inherent to the device structure and/or the measurement setup and are caused by current spreading (V_{CS}), thermoelectric voltages (V_T), input bias currents (V_{IBC}), or crosstalk and interference signals (V_{CI}). These four signals are normally quite insensitive to changes in the common-mode voltage in the transport channel, as explained in more detail in the Supplemental Material [44]. Therefore, the current source that is presented in this study will only have minor influence on these signals. Instead, the second group consists of charge-induced signals that are caused by the common-mode voltage within the nonlocal detection circuit. Therefore, our current source can be used to minimize their impact on nonlocal spin-transport measurements. This group includes signals that are caused by leakage currents (V_L), a finite common-mode rejection ratio (V_{CMRR}), and the signal that scales with the measurement frequency and that can be explained by charging currents of capacitances in the detection circuit (V_{CC}).

We note that the respective contribution of each charge-related signal can vary quite significantly depending on details like device fabrication, properties of the investigated material, device geometry, measurement setup, and measurement technique. Usually, there are one or two dominating charge-related signals, whereas others might only get relevant for the most precise measurements, for which voltage signals slightly above the thermal noise floor are to be measured. In Sec. III we discuss how a magnetic-field-dependent measurement can be used to determine the charge-induced contribution to the total nonlocal signal and how this contribution can then be subtracted from the measurement to obtain the bare spin signal. Additionally, we explain possible pitfalls that may occur in such a procedure.

A. Current spreading (V_{CS})

One of the most documented charge signals unfortunately does not have a consistent name convention, but instead can be found by different names in the literature, such as “current spreading,” “baseline resistance,” or simply “ohmic contribution” [18,19,35,43,45–47]. Common to all publications about this charge signal is a spatially inhomogeneous, nonuniform injection of the charge current into the DUT, either via a sidearm of a Hall bar structure or a pinhole in the tunnel barrier of the injection electrode. This is illustrated in Fig. 2(a) in which I_- drains the current and V_- detects any voltage uniformly over the whole width of the DUT. Electrode I_+ instead injects the current in a pointlike manner, breaking the spatial symmetry. A small part of the sourced current will flow on a curved path from I_+ into the nonlocal part of the device before it eventually flows into I_- . This leads to a nonuniform potential landscape in the nonlocal part of the device (colored lines illustrate equipotential lines; actual simulations of this effect can be found in Refs. [19,35,43,48]). This nonuniform potential landscape results in a potential difference V_{CS} between the two voltage probes V_+ and V_- (especially if V_+ also probes in a pointlike manner).

An out-of-plane magnetic field (as applied in a Hanle spin precession measurement) acts on the charge currents via a Lorentz force that modifies the potential landscape and therefore the measured nonlocal voltage [an illustration of the resulting change in the potential landscape is shown by dashed lines in Fig. 2(a)]. Numerical simulations have shown that this Hall-like effect can explain the background signal in Fig. 1(e) that depends both on the magnetic field and the charge carrier density [19,43]. In the case of a Hall bar geometry, the magnitude of the nonlocal charge signal at $B = 0$ T can be estimated by the van der Pauw theorem to [18]

$$V_{CS} = I\rho \exp\left(-\pi\frac{L}{w}\right) \quad (2)$$

with the applied current I , the two-dimensional sheet resistance ρ , the distance L between the sidearm at which the current is injected and the sidearm at which the nonlocal voltage is probed, and the width w of the transport channel.

We are not aware of a measurement technique that can minimize the contribution of V_{CS} to the overall nonlocal signal. Nevertheless, certain changes in the fabrication process can minimize this charge signal. Foremost, according to Eq. (2), an increase in the aspect ratio L/w can significantly reduce the effect of current spreading in both the cases of Hall bar and spin-valve geometries. As both the signal due to current spreading and the spin signal decay exponentially with the distance L between the I_+ and V_+ electrodes [1–3], it is especially the width w of the transport channel that should be minimized. Only applicable to the spin-valve geometry is the improvement of

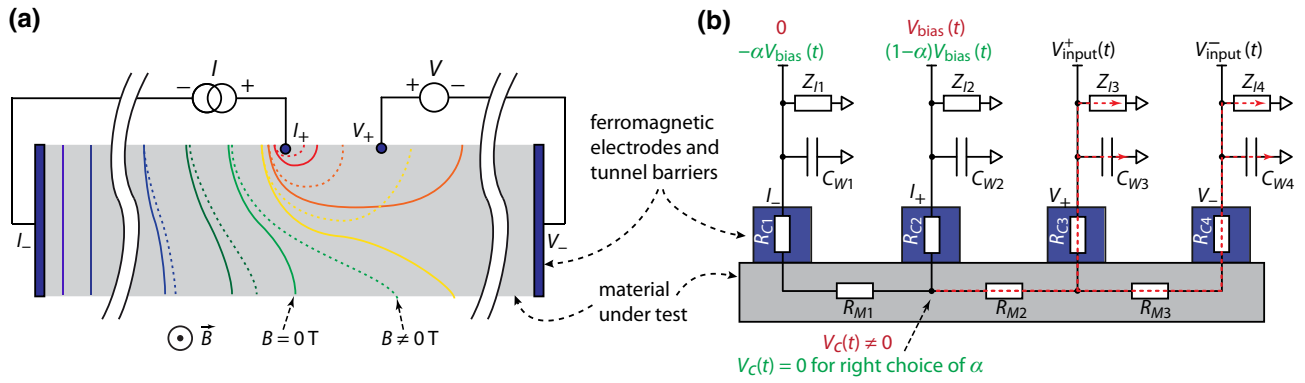


FIG. 2. (a) Schematic top view of the transport channel illustrating the effect of current spreading. Because of a spatially asymmetric injection of charge carriers, a small part of the overall current flows on a curved path from I_+ into the nonlocal part of the device before it drains into I_- . This leads to a measurable potential difference between the two voltage probes V_+ and V_- (colored lines illustrate equipotential lines), which can be changed by an out-of-plane magnetic field (dashed lines). (b) Simplified equivalent circuit of both the device under test and the measurement setup. Considered are the contact resistances R_{C_i} , the resistances R_{M_i} of the material, the capacitances C_{W_i} of the wiring, and the input impedances Z_{I_i} of the measurement equipment. The bias voltage $V_{\text{bias}}(t)$ that is necessary to drive a current through the injection circuit can, in principle, be freely distributed ($0 \leq \alpha \leq 1$) between electrodes I_+ and I_- . However, there is only one value of α , which depends on the voltage divider consisting of R_{C1} , R_{M1} , and R_{C2} , that shifts the whole nonlocal part of the device into a virtual ground (green letters). For every other setting of α , a nonzero common-mode voltage $V_{\text{CM}}(t) \neq 0$ will drive currents over every component that is referenced to ground in the nonlocal part of the device (red arrows).

the interface between the ferromagnetic electrode and the material under test (e.g., by minimizing pinholes in a tunnel barrier), to increase the uniformity of the charge carrier injection over the whole width of the transport channel.

B. Thermoelectric voltages (V_T)

It is well documented that thermoelectric and even magnetothermoelectric effects can cause nonlocal charge signals via a combination of Joule heating, the Peltier effect, the Seebeck effect, the Ettingshausen effect, or the Nernst effect [46,49–55]. The heat that is generated by the flow of charge carriers between the injection electrodes I_+ and I_- [Fig. 1(a)] creates a temperature gradient along the nonlocal part of the device, especially as electrodes V_+ and V_- can act as heat sinks. This temperature gradient then results in a differential voltage V_T via, e.g., the Seebeck or Nernst effect [49–55].

The heat that is created by the flow of charge carriers in the injection circuit can depend both linearly (e.g., in the case of the Peltier effect) or quadratically (e.g., in the case of Joule heating) on the applied current. Hence, in a lock-in measurement the resulting thermoelectric signal can appear both at the first and the second harmonic of the excitation frequency of the current [49,50]. To our knowledge, no phase shift is observed between the applied current and the thermally induced voltage. This is consistent with the thermal diffusivity of typical materials that are used for spin-transport devices [56,57]. These thermal diffusivities yield heat transfer times over the whole device that are several orders of magnitude shorter than the period

of typically applied ac signals (see a similar discussion about the spin diffusion coefficient in Sec. I).

Because of the inherent nature of thermoelectric voltages, we are not aware of measurement methods that can reduce their contribution after device fabrication. A suppression of these spurious signals can only occur by design choices during the fabrication process, like the design of electrodes that may function as heat sinks, the heat conductivity of the underlying substrate, or the design of the I_+ and I_- electrodes in such a way that their respective Peltier effects cancel each other to some extent [46,54,55].

Finally, it is important to note that thermoelectric signals not only depend on gate-induced changes in the transport properties of the DUT [58,59], but that there are even magnetic-field-dependent analogs to the Peltier and Seebeck effects, which are the Ettingshausen and Nernst effects, respectively. These two effects can result in a B -field dependence of the corresponding nonlocal, thermoelectric signal [49,51,52].

C. Input bias currents (V_{IBC})

We now assume that no current source is connected to the device and that the electrodes I_+ and I_- are shorted to ground. The only equipment that is connected to the DUT via electrodes V_+ and V_- is either a differential voltage amplifier or a lock-in amplifier. But even in this situation a small current will flow through the device. This is due to currents that are flowing either out of or into the inputs of a voltage or a lock-in amplifier. Especially in the case of operational amplifiers or instrumentation amplifiers this current is called input bias current [60–62]. In a transport

measurement these input bias currents result in nonlocal charge currents and, therefore, generate voltage drops V_{IBC} within the device.

The input bias currents differ by several orders of magnitude between different measurement equipments. Because of high input bias currents up to the nanoampere or even microampere range, standard amplifiers that use bipolar junction transistors (BJTs) in their input stages are unsuitable for nonlocal spin measurements. However, precision amplifiers may include internal circuitry that diminishes the input bias currents of BJT inputs down to the higher picoampere range. Even lower input bias currents in the lower picoampere or even femtoampere range [63] can be found in amplifiers that use field-effect transistors. However, even this type of amplifier might cause problems, as damage to the input stages may increase these currents significantly.

It is *a priori* not clear if the charge signal that is caused by input bias currents is relevant in a nonlocal spin measurement. We recommend to measure both the input bias currents and the CMRR (see Sec. II G) of the experimental setup to clarify this point. In the Supplemental Material [44] we give more information about such measurement procedures and discuss why input bias currents are normally only relevant for dc measurements.

D. Crosstalk and interference signals (V_{CI})

There is always a certain coupling between different signal lines within a measurement setup. Especially cryogenic measurement systems, for which unshielded cables are often placed close together over longer distances [64], can exhibit non-negligible capacitive coupling between individual lines. An ac signal, like the bias voltage that drives the current through the injection circuit, can therefore couple into the wires that are connecting the V_+ and V_- electrodes to the measurement equipment outside the cryostat. Everything that will change the amplitude of the bias voltage, like a gate-induced change in the conductance of the DUT or a magnetoresistance effect, can change the amplitude of the signal V_{CI} that is coupled into the nonlocal detection circuit.

Wires can also be prone to damage to their insulation, which can yield reduced insulation resistances between different lines. Leakage currents directly between wires of the injection and detection circuit can therefore result in spurious signals in the cases of both ac and dc measurements. Fortunately, such setup-related signals can be easily identified by measuring the impedances between each line without any installed DUT.

Interference signals that couple from external sources into the measurement setup can also result in spurious, nonlocal signals. A common but erroneous assumption is that radio frequency (rf) signals do not impact dc or

lock-in measurements, as in the first case the signal is averaged over timescales several orders of magnitude longer than the period of the rf signal and in the second case the lock-in only measures a signal within a very narrow band around the excitation frequency. But as long as there are nonlinear components within the measurement circuit, a down-mixing of the rf interference signal occurs. As a result, rf signals are known to, e.g., create dc offset voltages in amplifier circuits [65–67].

E. Common-mode voltage and virtual ground

All of the nonlocal charge signals, which are discussed in the following sections, significantly depend on the so-called common-mode voltage $V_{CM}(t)$ in the nonlocal part of the device. This is the voltage that is common to both inputs [noninverting (+) and inverting (–) inputs] of the differential amplifier that is connected to electrodes V_+ and V_- . If we denote these input voltages as $V_{input}^{+/-}$ then the common-mode voltage is defined as

$$V_{CM}(t) = \frac{V_{input}^+(t) + V_{input}^-(t)}{2}. \quad (3)$$

To simplify the discussion on this matter, we make several assumptions that should apply well to a majority of devices. However, these assumptions should be carefully examined considering own device schemes and measurement techniques.

We assume that the frequency of the applied ac current is low enough that any inductance or capacitance of the DUT can be neglected, while the measurement setup can still exhibit inductances or capacitances. The analog assumption in the case of a dc measurement is that the time step between two measurement points is much longer than the settling time that is caused by the inductance or capacitance of the DUT. Accordingly, we model the equivalent circuit of the device by a series of ohmic resistors [Fig. 2(b)] where the contact resistances R_{Ci} exhibit ohmic characteristics. Finally, we assume that the measurement system exhibits a well-defined ground (GND) potential, that every voltage is referenced to this GND, and that the shielding of any coaxial cables are put to the same GND.

To drive a current I_{bias} through the injection circuit, a current source has to apply the voltage

$$V_{bias} = I_{bias}(R_{C1} + R_{M1} + R_{C2}) \quad (4)$$

between electrodes I_+ and I_- . The easiest way to accomplish this is to put one of the electrodes to GND and to apply the full bias voltage (referenced to GND) to the other electrode [red letters in Fig. 2(b)]. Because of the voltage divider that is built from R_{C1} , R_{M1} , and R_{C2} , the material under test right below the injection electrode I_+ will be on a potential $V_c(t)$ that is unequal to zero, i.e., unequal to GND. Every measurement parameter that has an effect on

one of the resistances R_{C1} , R_{M1} , and R_{C2} will thus have an impact on $V_c(t)$. For example, changing the conductivity of the material by tuning the charge carrier density via a gate voltage will change R_{M1} . Therefore, all spurious nonlocal signals that are caused by $V_c(t)$ will show a gate-dependent behavior.

If we neglect any charge currents and their associated ohmic voltage drops in the nonlocal part of the device, the same voltage $V_c(t)$ is applied to both inputs of the differential voltage amplifier that is connected to electrodes V_+ and V_- . Under this condition, the common-mode voltage $V_{CM}(t)$ would be equal to $V_c(t)$.

As explained in the following sections, several nonlocal signals are caused by this common-mode voltage. Fortunately, there is a quick way to check if V_{CM} is playing a role in a measurement. For the wiring denoted with the red letters in Fig. 2(b), the measurement only has to be repeated after putting a high-ohmic resistor between the L_- electrode and GND. The current-induced voltage drop over this additional resistor will lift the potential (measured against GND) in the whole circuit, therefore increasing V_{CM} . There is only one pitfall to this method, which is a general problem for nonzero common-mode voltages in devices in which the charge carrier density is controlled via electrostatic gating: gate voltages are normally referenced to GND, but the gate-electric field effect does not depend on the absolute value of the gate voltages but the potential differences between the gates and the DUT. Changing V_{CM} is therefore also changing the gate-induced charge carrier densities (see the Supplemental Material [44] for more information). If the spin signal depends on the charge carrier density, it might be difficult to tell if a change in the nonlocal signal by lifting the nonlocal part of the DUT to another potential is related to either a change in the charge-carrier-dependent spin signal or a change in the common-mode-dependent spurious signals.

The current source that is presented in this work can significantly reduce the common-mode voltage by freely distributing the potential difference that is necessary to drive the current to the two injection electrodes [green letters in Fig. 2(b)]:

$$V_{\text{bias}}(t) = [(1 - \alpha)V_{\text{bias}}(t)] - [-\alpha V_{\text{bias}}(t)] \quad (5)$$

with α adjustable between $0 \leq \alpha \leq 1$ (see the in-depth technical discussion of the current source in the Supplemental Material [44]). Depending on the values of the ohmic voltage divider consisting of R_{C1} , R_{M1} , and R_{C2} , there will be a certain value of α for which the common-mode voltage is zero [$V_{CM}(t) = 0$]. Although the nonlocal part of the device is not connected to GND, it will nevertheless be on ground potential at all times. The right choice of α will therefore create a so-called virtual ground in the nonlocal part of the device. This not only nullifies the nonlocal charge signals that are caused by V_{CM} ,

but also results in the fact that any applied gate voltage (referenced to GND) is equal to the potential difference between gate and the nonlocal part of the DUT (see the Supplemental Material [44] on how the adjustment of α therefore also impacts a local four-probe measurement of the gate-dependent resistivity of graphene).

F. Voltages caused by leakage currents (V_L)

The most obvious nonlocal charge signal that is caused by a common-mode voltage V_{CM} is due to leakage currents to GND. Especially the finite input impedances of measuring equipment [Z_{Ii} in Fig. 2(b)] play a crucial role, but also more unexpected current paths to GND like damaged insulation of cables or broken capacitors. These leakage currents [red, dashed lines in Fig. 2(b)] create ohmic voltage drops over the resistances R_{C3} , R_{M3} , and R_{C4} , which result in a nonlocal voltage V_L between V_+ and V_- .

Assuming purely ohmic impedances and a voltage divider model, the amplitude of this nonlocal voltage scales linearly with the common-mode voltage V_{CM} and significantly depends on the relative magnitude of the leakage resistance to ground with respect to the resistances R_{C3} , R_{M3} , and R_{C4} . Therefore, it is not surprising that spurious voltage signals due to leakage currents are mainly reported in measurements of high-impedance states (see Ref. [68] and the supplementary information of Refs. [10,11]). Hence, the spurious signal V_L can, e.g., be much more pronounced in graphene-based spin valves, in which high-resistive tunnel barriers have to be incorporated to overcome the conductivity mismatch problem [69–71] compared to metallic spin valves without tunnel barriers.

In our work on graphene-based spin valves, we use a lock-in amplifier that has an input impedance of only 10 M Ω to GND (SR830 from Stanford Research Systems). To reduce the effect of leakage currents, we use an additional differential amplifier (SR560 from Stanford Research Systems) with a higher input impedance of 100 M Ω to probe the differential voltage between electrodes V_+ and V_- before the nonlocal signal is sent to the input of the lock-in [Fig. 1(a)]. Some laboratory-grade multimeters and voltmeters even offer the possibility to select the input impedance to be either 10 M Ω or 10 G Ω . Repeating a nonlocal measurement with different input impedances can easily answer the question if the measured nonlocal voltage is partially caused by leakage currents. But the best solution is to avoid leakage currents entirely by creating a virtual ground inside the nonlocal part of the device. Under such conditions, the absence of a potential difference between the nonlocal part of the device and GND completely prevents leakage current from flowing.

G. Common mode rejection ratio (V_{CMRR})

The output voltage $V_{\text{out}}^{\text{ideal}}$ of an ideal differential voltage amplifier, which has a differential gain of G_{diff} and

is connected to electrodes V_+ and V_- [Fig. 1(a)], is given by

$$V_{\text{out}}^{\text{ideal}} = G_{\text{diff}}(V_{\text{input}}^+ - V_{\text{input}}^-). \quad (6)$$

However, the output voltage $V_{\text{out}}^{\text{real}}$ of a real differential amplifier also contains a contribution that is proportional to the average voltage at electrodes V_+ and V_- and that scales with the common-mode gain G_{CM} [60,61,63,68,72,73]:

$$V_{\text{out}}^{\text{real}} = G_{\text{diff}}(V_{\text{input}}^+ - V_{\text{input}}^-) + G_{\text{CM}} \frac{(V_{\text{input}}^+ + V_{\text{input}}^-)}{2}. \quad (7)$$

Neglecting any current-driven voltage drops in the nonlocal part of the device, the average voltage of electrodes V_+ and V_- is exactly the voltage that is denoted as the common-mode voltage V_{CM} in Sec. II E. Therefore, V_{CM} will appear in the nonlocal measurement, although strongly attenuated by the common-mode gain G_{CM} . Data sheets of measurement equipment often state the ratio between the differential and the common-mode gain, the so-called common-mode rejection ratio (CMRR):

$$\text{CMRR} \left[\frac{\mu\text{V}}{\text{V}} \right] = \frac{G_{\text{diff}}}{G_{\text{CM}}}, \quad \text{CMRR}[\text{dB}] = 20 \log \left(\frac{G_{\text{diff}}}{G_{\text{CM}}} \right). \quad (8)$$

In some data sheets the CMRR is only given for a specific differential gain and measurement frequency. As the CMRR can depend quite significantly on these two parameters, it is always good practice to measure the CMRR of the own setup at gains and frequencies used for the experiments.

H. Capacitor charging (V_{CC})

All previously discussed signals are in phase with the current that is flowing in the injection circuit and are thus in phase with the spin signal. In contrast, the charge signal that is discussed in this section is phase shifted to values close but unequal to 90° . If a sinusoidal current is driven through the injection circuit, $V_{\text{CM}}(t)$ and, therefore, the whole potential of the nonlocal part of the device will also change sinusoidally over time. This is a problem as there are capacitances to GND in the nonlocal detection circuit [C_{W3} and C_{W4} in Fig. 2(b)]. Some of these capacitances are intentional, like the capacitors of RC low-pass filters, others are either parasitic or unavoidable, like capacitances to GND of the wiring (around 100 pF/m in the case of coaxial cables) or the input capacitance of measurement equipment. As a result, the time-varying common-mode voltage $V_{\text{CM}}(t)$ will drive charge and discharge currents over these capacitors [dashed red lines in Fig. 2(b)].

The resulting differential voltage V_{CC} between V_+ and V_- can be best understood if the combinations of the

device resistances (R_{Ci} and R_{Mi}) and the setup capacitances (C_{Wi}) are seen as RC low-pass filters for the voltage $V_c(t)$ in Fig. 2(b). The respective RC time constants of the low-pass filters of the voltage probes V_+ and V_- typically differ, i.e.,

$$(R_{M2} + R_{C3})C_{W3} \neq (R_{M2} + R_{M3} + R_{C4})C_{W4}. \quad (9)$$

As a result, both the amplitude and the phase of the transmitted voltage signal will differ between the two inputs of the differential voltage amplifier. This leads to a partial conversion of the common-mode voltage into a differential voltage, which is a well-known phenomenon in electronics. Such a conversion is discussed in many application notes of analog-to-digital converters, where a mismatch in the capacitors of a common-mode filter can convert common-mode noise into differential noise. Another example is the conversion between common- and differential-mode voltages caused by imbalances in filters against electromagnetic interference [74,75].

Although the voltage V_{CC} is caused by the charging currents of the capacitors C_{W3} and C_{W4} , it is nevertheless not perfectly at a phase of 90° relative to $V_c(t)$ due to the ohmic resistances R_{M2} , R_{M3} , R_{C3} , and R_{C4} . Therefore, V_{CC} also provides a contribution to the X -channel signal of the lock-in amplifier, which will be discussed in Sec. III and can also be seen in simulations conducted with LTspice (models used for the simulations are available in Ref. [76]).

The amplitude $M = \sqrt{X^2 + Y^2}$ of V_{CC} scales linearly with the measurement frequency (see Sec. III), because the current I_{cap} that is caused by a voltage $V_{\text{cap}}(t) = V_{\text{cap}}^0 \sin(\omega t)$ over a capacitor C is given as

$$I_{\text{cap}}(t) = C \frac{dV_{\text{cap}}(t)}{dt} = \omega C V_{\text{cap}}^0 \cos(\omega t). \quad (10)$$

This capacitor charging current also flows through the nonlocal part of the device. In general, V_{CC} is highly dependent on every change in the device's resistances and capacitances: a change in R_{C1} , R_{M1} , or R_{C2} will change the value of $V_c(t)$ and, therefore, also the voltage that will be applied to the capacitors C_{W3} and C_{W4} . On the other hand, every change in R_{M2} , R_{M3} , R_{C3} , R_{C4} , C_{W3} , or C_{W4} will have an impact on the RC time constants.

To minimize V_{CC} , the capacitances C_{W3} and C_{W4} should be minimized as much as possible, e.g., by reducing the length of the wiring from the V_+ and V_- electrodes or by avoiding any RC low-pass filters in the measurement setup. Furthermore, additional ohmic resistors might be put into series to the electrodes V_+ and V_- to roughly match the RC time constants by compensating varying contact resistances. But the best way to suppress V_{CC} is to set the whole nonlocal part of the device to a virtual ground. In such a case, there is no potential difference across the capacitors C_{W3} and C_{W4} and, therefore, no capacitor charging current.

I. Magnetic-field-dependent measurements

Magnetic-field-dependent transport measurements are usually performed to distinguish an actual spin signal from spurious charge signals. The success of such an approach significantly depends on two conditions.

1. Does the spin signal exhibit a magnetic field dependence that significantly differs from the magnetic response of the charge-induced signals? The best-case scenario here is the existence of a clear spin precession signal.

2. Does the experiment allow us to switch the orientation of the injected spins, e.g., by switching the magnetization of the ferromagnetic electrodes?

If both conditions are met, the most reliable way to mathematically remove any charge-induced contribution from the measured data is to record the Hanle spin precession curves for both parallel ($\uparrow\uparrow$) and antiparallel ($\uparrow\downarrow$) orientations of the respective magnetization of the injection and detection electrodes. In the ideal case only the bare spin signal V_S will change its sign when reversing the relative magnetization directions [1,2]. Instead, all other spin-independent, charge-induced signals in Eq. (1) should not change with the magnetization of the electrodes (exceptions are discussed further below). Therefore, the arithmetic mean of both measurements should yield the charge-induced background signal:

$$V_{\text{background}} = \frac{V_{\text{nl},\uparrow\uparrow} + V_{\text{nl},\uparrow\downarrow}}{2}. \quad (11)$$

This is shown as the green line in Fig. 1(e). Subtracting both measurements from each other should yield the pure spin signal

$$2V_S = V_{\text{nl},\uparrow\uparrow} - V_{\text{nl},\uparrow\downarrow}. \quad (12)$$

Under such conditions, the charge-induced signals should not pose any risk of a misinterpretation of the spin-dependent data. Nevertheless, the noise that is associated with the charge-induced signals cannot be removed by this subtraction method and, therefore, will deteriorate the signal-to-noise ratio of the spin signal.

It is important to note that Eqs. (11) and (12) are no longer valid if the ferromagnetic electrodes exhibit fringe or stray fields that can act on the DUT. Such fields are well known to complicate the analysis of spin measurements [23,48,77–81] and can appear in quite different forms. (1) As long as the width of the electrode is small enough that a single-domain magnetization prevails [42], fringe fields with relevant strengths should only be located at the electrode's two faces that are normal to the electrode's easy axis [42,82]. Stray fields can impact the measurement if these two faces are placed too close to or even on top of the transport channel [23,77,78]. (2) If the width

of the electrode is too wide, the magnetization can fall into a multidomain structure that exhibits stray fields all along its different faces [42]. (3) A magnetic field applied noncolinear to the electrode can rotate the magnetization from the electrode's easy axis [41], possibly pushing fringe fields towards the transport channel. This can lead to a situation where fringe fields increasingly affect the DUT with increasing external magnetic field strength (see the main text and the supplementary information of Refs. [28,48,83]). (4) Stray fields can also occur if the surface of the ferromagnet exhibits a great roughness, which, e.g., can be caused by pinholes in a tunnel barrier that is separating the ferromagnet from the DUT [79–81]. (5) Stray fields can also be created by domain walls that are pinned at steps in the ferromagnetic electrode. Even the small height difference between a substrate and the top of a single layer graphene spin valve was found to be large enough to be able to pin a domain wall [82].

Fringe or stray fields can become a real issue if there is no unmistakable signature of spin precession in a magnetic-field-dependent measurement. For example, in three-dimensional topological insulators (TIs) spin precession in a nonlocal spin-transport measurement is not expected because of the spin-momentum locking [84]. This is the reason why only spin-valve measurements are shown in a large number of publications about spin-transport experiments in TIs [85–91]. In this context, it was indeed demonstrated that fringe-field-induced Hall voltages can create artifacts that resemble the switching signals that are expected from a current-induced spin polarization in TI-based spin valves [23,77,81].

If neither of the two above conditions is fulfilled, it is even more important to carefully analyze the nonlocal spin measurements to avoid a misinterpretation of the results. This is especially the case for nonlocal spin Hall experiments, for which quite controversial results have been published over the years [4]. In particular, reports about unexpectedly large spin Hall effects [92–94] often could not be reproduced in later studies that instead identified the role of charge-induced signals in the nonlocal measurement [18–22].

Unfortunately, many studies only consider the one charge-induced signal that contributes the most to the overall nonlocal signal. After subtracting this spurious signal from the measured data, it is then argued that the remaining signal has to be due to spins, especially when the signal shows a magnetic field dependence. However, quite a few charge-induced signals can also exhibit a magnetic field dependence: all charge currents that are flowing in the nonlocal part of the device, either caused by current spreading or leakage currents, experience the Hall effect. Furthermore, thermal voltages due to the Ettingshausen and Nernst effects show a magnetic field dependence. And, finally, any magnetoresistive effect that changes the resistance of the DUT in the injection circuit [R_{M1} in Fig. 2(b)] will have

an impact on the common-mode voltage V_{CM} and, therefore, will change all charge-induced signals that depend on V_{CM} , i.e., V_L (Sec. II F), V_{CMRR} (Sec. II G), and V_{CC} (Sec. II H). The magnetic-field-induced changes might be small, but so are the majority of measured nonlocal spin signals.

III. PHASE-SHIFTED CHARGE SIGNAL IN LOCK-IN MEASUREMENTS

In this section, we discuss in detail the charge-induced nonlocal voltage signal that is caused by the charging and discharging currents of the capacitances in the nonlocal part of the setup (see Sec. II H). For this purpose, we measure graphene spin-valve devices with cobalt electrodes and either MgO or Al₂O₃ tunnel barriers (details on the exact device geometry and the fabrication process including flake transfer techniques, etching recipes in the case of structured CVD-graphene devices, and metalization schemes can be found in Refs. [36,37,95–99]). Figures 3(a) and 3(b) demonstrate how a change in the RC time constant of the V_+ electrode has a direct impact on the spin-valve signal in both the X and Y channels. For this experiment, α is not adjusted to create a virtual ground in the nonlocal part of the device (see the explanation in

Sec. II E). Instead, α is arbitrarily set to $1/2$, which resulted in a nonvanishing common-mode voltage $V_{CM}(t)$ in this device [Fig. 2(b)].

The manipulation of the RC time constant is accomplished both by connecting ohmic resistors in series to the contact resistance of the V_+ electrode [resistance values in Figs. 3(a) and 3(b)] and by increasing the length of the coaxial cable that is connecting the electrode to the differential voltage amplifier (100 pF per meter). These manipulations do not have any impact on the amplitude of the spin signal [switching in Fig. 3(a) indicated by the dashed arrows], but create an ever increasing offset in the signal of the X channel. As the charge signal is shifted in phase by almost 90° , the increase in the Y -channel signal [Fig. 3(b)] is significantly more pronounced. In fact, after applying a differential gain of $G_{diff} = 1000$ by the voltage amplifier [see Fig. 1(a)], the voltage measured by the Y channel of the lock-in eventually reaches 1 V, which is the maximum voltage before the input of the used lock-in goes into an overload condition.

Simulations conducted with LTspice [76] confirm the dependence of the nonlocal charge signal on variations in the resistances of the contacts and the capacitances of the wiring. The equivalent circuit for this simulation is shown

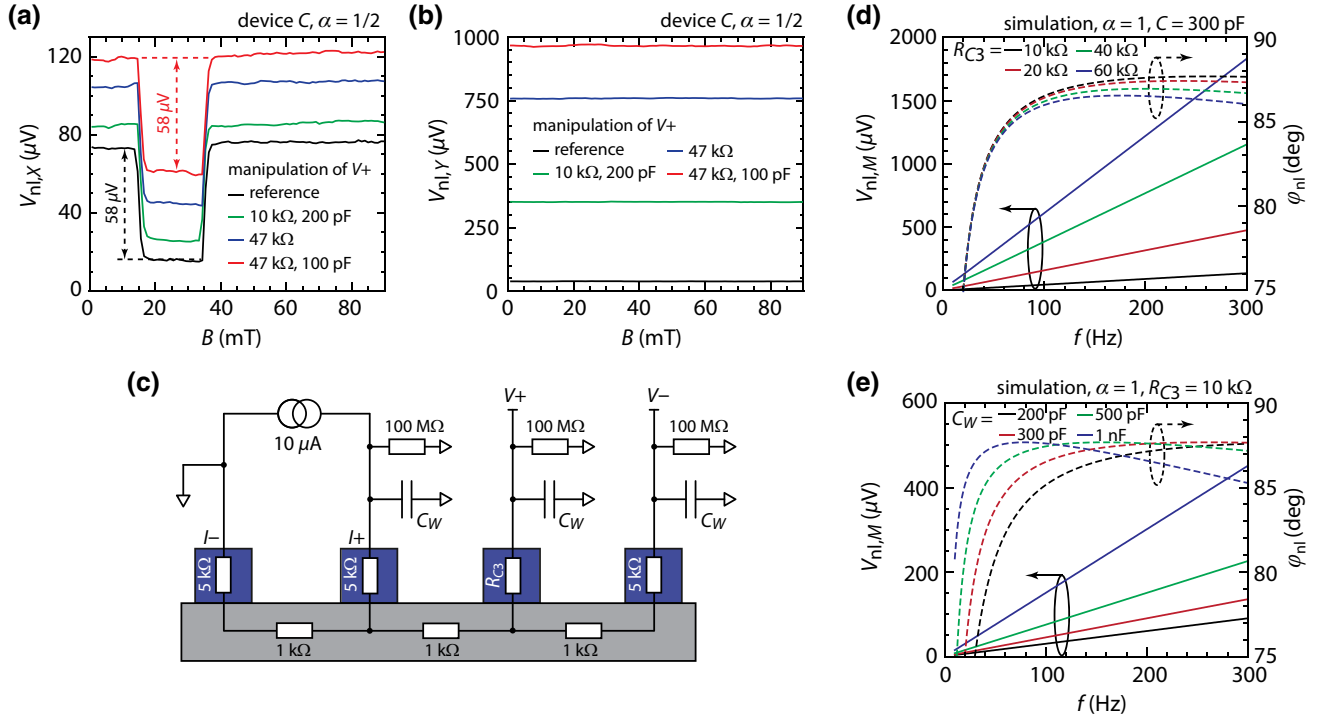


FIG. 3. Demonstration on how changing the RC time constant of the V_+ electrode impacts the measured nonlocal voltage. (a),(b) Spin-valve measurements are repeated with additional resistors and BNC cables (100 pF/m) connected to the V_+ electrode. The impact on the recorded nonlocal signal is depicted in panel (a) for the X channel and in panel (b) for the Y channel of the lock-in. (c) Equivalent circuit that is used to simulate the effect of varying RC time constants. (d) Corresponding amplitude $M = \sqrt{X^2 + Y^2}$ and phase of the nonlocal voltage measured between V_+ and V_- if the resistance R_{C3} in (c) is varied for a fixed capacitance C_W of the external wiring. (e) Same as in panel (d) but for a fixed value R_{C3} and different values for C_W .

in Fig. 3(c), where either the contact resistance R_{C3} or the capacitance C_W of the wiring is varied, whereas all other values are set to parameters typical for a graphene-based spin-valve device (LTspice files can be found in Ref. [76]). From the simulations, the amplitude $M = \sqrt{X^2 + Y^2}$ and the phase φ_{nl} [see the definitions in Fig. 1(c)] of the differential, nonlocal voltage $V_{nl} = V_+ - V_-$ is extracted as a function of the driving frequency f of the current in the injection circuit. Figure 3(d) shows the results for different values of R_{C3} and a fixed capacitance of $C_W = 300$ pF, while Fig. 3(e) depicts the case with a fixed contact resistance $R_{C3} = 10$ k Ω but varying capacitances C_W . Both cases demonstrate the linear increase in the amplitude of the nonlocal charge signal with the measurement frequency (see the explanation in Sec. II H). Furthermore, the simulations demonstrate that the resulting nonlocal charge signal has a phase close to but not exactly at 90° due to the ohmic contributions. The strongly decreasing phase towards lower frequencies is caused by the frequency-independent leakage currents that are flowing over the finite input impedances that are modeled by the 100 M Ω resistors (see Sec. II F). As soon as the signal that is caused

by the capacitor charging becomes negligible towards $f = 0$ Hz, the leakage currents, which are in phase with the current in the injection circuit, are eventually dominating and pushing the phase to zero.

The experimental results and simulations shown in Fig. 3 demonstrate how much the measurement signal can depend on the wiring of the measurement setup. In particular, RC low-pass filters can be extremely disadvantageous to nonlocal, lock-in-based measurements, as they significantly increase the total capacitance of the V_+ and V_- lines to GND. This in turn increases the spurious signals that are caused by the charging currents of the corresponding capacitors. We use the equivalent circuit that is shown in Fig. 4(a) to simulate how a mere change of the DUT's resistances ($R_{Mi} = R_M$ for $i = 1, 2, 3$) impacts the nonlocal signal. In this equivalent circuit the charge signal is intentionally diminished by assuming identical values for contact resistances, capacitances of the wiring, and RC filter characteristics for all relevant contacts. Therefore, the only difference in the overall RC time constants of contacts V_+ and V_- is given by the value of $R_{M3} = R_M$. Of course, the resistance $R_{M1} = R_M$ in the injection circuit

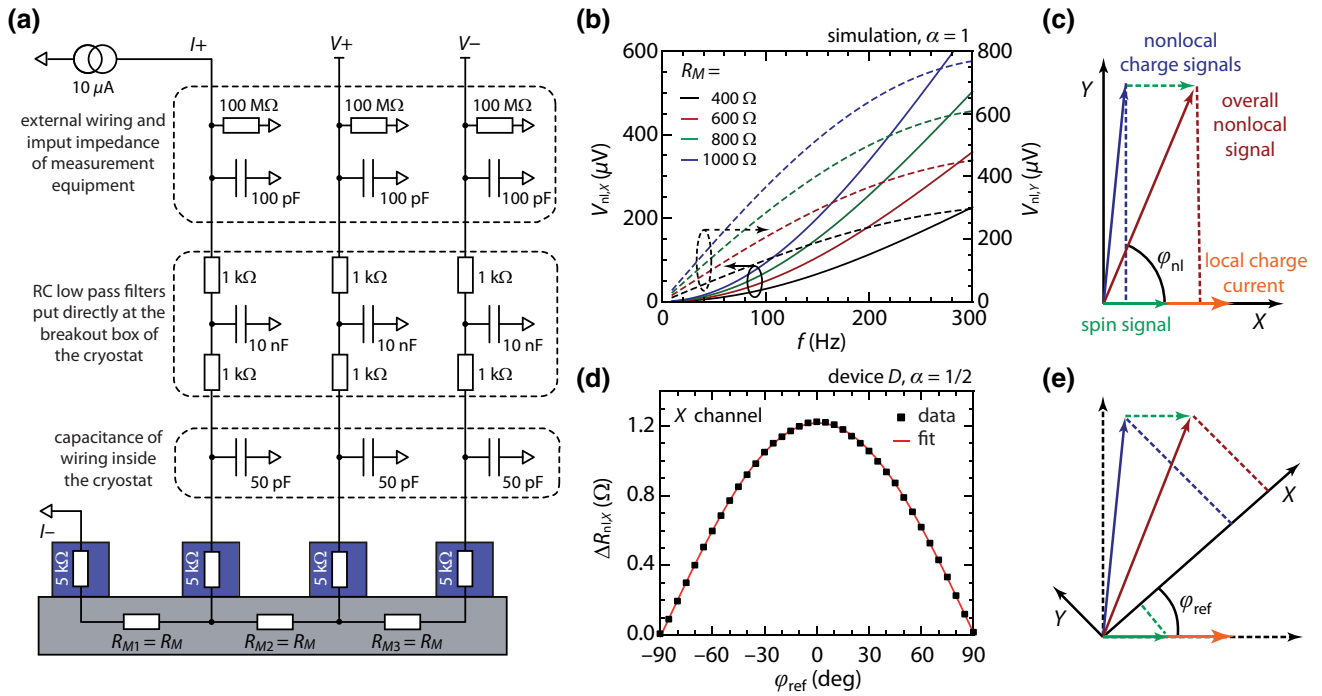


FIG. 4. (a) Equivalent circuit that is used to simulate the detrimental impact of additional RC low-pass filters on the nonlocal spin measurement. The high capacitances to ground of these filters significantly increase the spurious nonlocal signals that are caused by the charging and discharging currents over these capacitors. (b) The simulated signals in the X channel (solid lines) and Y channel (dashed lines) as a function of the applied measurement frequency for different resistances R_M of the material. (c),(e) To verify that the readout of the X channel actually captures the whole spin signal, a rotation of the coordinate system by a reference phase φ_{ref} can be utilized. As only the projection of each signal on the respective axis is measured, the amplitude of the spin signal should decrease as soon as the X axis is rotated. (d) Corresponding experiment in which the amplitude of the spin-related switching in a spin-valve measurement is recorded as a function of φ_{ref} . The maximum around 0° demonstrates that the presented current source creates a current signal and, therefore, a spin signal that is in phase with the output of the lock-in [compare to Fig. 1(a)].

also influences the common-mode voltage V_{CM} that is driving the nonlocal currents in the first place. In Fig. 4(b) the resulting nonlocal charge signals for both the X channel (solid lines) and Y channel (dashed lines) are plotted as a function of the measurement frequency for different values of R_M . The results strikingly demonstrate how significantly the spurious nonlocal charge signal depends in this case even on gate-induced changes in the DUT's resistivity. The simulations are conducted with an applied current of $I = 10 \mu\text{A}$; therefore, the left y axis in Fig. 4(b) corresponds to a nonlocal resistance between 0 and 60 Ω .

The example of the RC filters illustrates how drastically specific details of the setup can influence such measurements. We therefore strongly advise verifying the basic assumptions that are often made for individual setups. One important assumption is that the spin signal is fully located within the X channel of the lock-in. As discussed in Sec. I, the spin signal should be in phase with the current in the injection circuit, which in turn should be in phase with the output signal from the lock-in's internal oscillator [green and orange vectors in Fig. 4(c)]. Instead, the vector addition of all nonlocal charge signals results in a signal with a phase somewhere between 0° and 90° [blue vector in Fig. 4(c)].

Most lock-in amplifiers offer the possibility to rotate the X - Y -coordinate system by a reference phase φ_{ref} relative to the internal oscillator, which is illustrated in Fig. 4(e). The measured signals are then the projections of both the spin and charge signals onto the respective axis. The amplitude of the actual spin signal in the X channel as a function of φ_{ref} can be determined by the amplitude of the switching in a spin-valve measurement that is repeated for different φ_{ref} [43]. In the case of our setup and the newly designed current source, the result of such an experiment is shown in Fig. 4(d). The actual data points (black squares) can be perfectly fitted (red line) with an equation that describes the projection of the spin signal onto the rotating X axis:

$$\Delta R_{\text{nl},X}(\varphi_{\text{ref}}) = \Delta R_{\text{nl},X}^0 \cos(\varphi_{\text{ref}} - \varphi_{\text{off}}) \quad (13)$$

with a maximum spin signal $\Delta R_{\text{nl},X}^0$ and an offset phase φ_{off} between the spin signal and the internal oscillator signal. The fit yields a value of $\varphi_{\text{off}} = 0.6^\circ$ that demonstrates that our current source creates a current signal and, therefore, a spin signal that is almost perfectly in phase with the output of the lock-in.

Finally, we demonstrate the actual strength of such a current source: the distribution of the bias voltage between contacts I_+ and I_- can be controlled in a way that the nonlocal part of the device is set to a virtual ground (see the theoretical explanation in Sec. II E and the discussion about the technical operation of the current source in the Supplemental Material [44]). Under this condition, the common-mode voltage in the nonlocal part is zero at all times [$V_{\text{CM}}(t) = 0$], i.e., no charge current can flow over

any resistance or capacitance to GND. Furthermore, spurious signals due to a finite common-mode rejection ratio of the measurement setup are also minimized.

The impact of such an adjustment procedure on a Hanle measurement is shown in Fig. 5(a). The particular device for this demonstration was chosen because it only exhibits a constant background signal, which is typical for the capacitor charging effect. The absence of a magnetic-field-dependent background indicates that the current spreading effect is largely diminished. The red lines depict Hanle curves in both parallel (solid lines) and antiparallel (dashed lines) magnetization configurations of the I_+ and V_+ electrodes if a symmetric bias is applied to electrodes I_+ and I_- [$\alpha = \frac{1}{2}$, i.e., $\frac{1}{2}V_{\text{bias}}(t)$ to I_+ and $-\frac{1}{2}V_{\text{bias}}(t)$ to I_- ; compare to Fig. 2(b)]. As the growth of uniform and reproducible tunnel barriers on the inert graphene is quite challenging [27,100–103], the difference in the respective contact resistances of I_+ and I_- is usually quite large. Therefore, the virtual ground point in the case of a symmetric bias voltage normally does not lie within the transport channel of the DUT. Accordingly, there is a finite common-mode voltage $V_{\text{CM}}(t)$ driving the spurious nonlocal signals, which is seen as a background signal. Instead, the green curves in Fig. 5(a) depict the same Hanle measurement (recorded in the X channel) after α is adjusted in such a way that the signal in the Y channel of the lock-in is minimized. With this adjustment, the background signal in the Hanle measurement has also almost completely vanished (in the Supplemental Material [44] we demonstrate that adjusting α until the signal in the Y channel is minimized also avoids common-mode related artifacts in local measurements).

The dependence of the nonlocal signal on the frequency is depicted in Figs. 5(b) and 5(c) for the X channel and Y channel, respectively. For these graphs, the values in the parallel configuration of the Hanle curves at $B = 0$ T are measured for both the symmetric (red) and the adjusted bias conditions (green). In the Y channel [Fig. 5(c)] the aforementioned linear increase of the charge-induced, nonlocal signal with increasing frequency can be observed in the case of the symmetric bias condition. At a frequency of $f = 300$ Hz the charge-induced signal is already over 30 times larger than the actual spin signal in the X channel. For more unfavorable values of α or in devices that have even more strongly varying contact resistances, the charge-induced signal can even be much larger. This and the fact that spin signals can be much smaller than that presented in Fig. 5 can yield huge differences between the amplitudes of the spin and charge-induced signals of up to several orders of magnitude.

It is important to note that the charge-induced signal in Fig. 5(c) goes to zero for $f \rightarrow 0$ Hz even in the case of $\alpha = \frac{1}{2}$. This implies that the complete signal in the Y channel is caused by the capacitor charging effect, as its amplitude scales linearly with the applied frequency (see the explanation in Sec. II H). On the other hand, in Fig. 5(b)

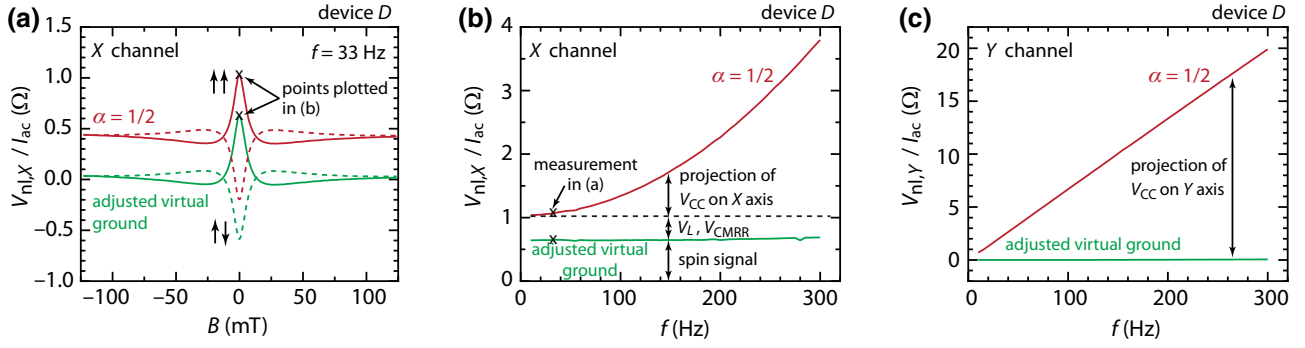


FIG. 5. Demonstration that charge-induced signals can be significantly reduced by adjusting the virtual ground with the help of the presented current source. (a) Hanle curves measured with a symmetric bias applied to electrodes I_+ and I_- (red curves) show a distinct background signal. Instead, the green curves depict the same Hanle measurement after the nonlocal part of the device is put to a virtual ground. This prevents the flow of any charge current in the detection circuit over resistances or capacitances to ground and, therefore, diminishes the charge-induced background signals. (b),(c) Nonlocal signal as a function of measurement frequency for both the X channel (b) and the Y channel (c). For these graphs, the values in the parallel configuration of the Hanle curves at $B = 0$ T are measured for both bias conditions. In the case of a symmetric bias voltage, the charge-induced signal gets much larger than the actual spin signal, especially in the Y channel. Instead, in the case of the adjusted virtual ground, the signal in the Y channel is negligible over the whole measurement range and the signal in the X channel consists of only the actual spin signal.

there is still an offset between the two curves for $\alpha = \frac{1}{2}$ and the adjusted ground condition for $f \rightarrow 0$ Hz (indicated by the dashed line). That means that there are additional charge-induced signals present in the X channel, apart from the projection of V_{CC} onto the X channel that is responsible for the increasing background signal towards higher frequencies. This increase is not linear as the increase seen in Fig. 5(c), because the overall phase of V_{CC} varies slightly with the applied frequency [see the frequency-dependent phases in Figs. 3(d) and 3(e), and the nonlinear increase of the signal in the X channel in Fig. 4(b)]. Importantly, adjusting the virtual ground in such a way that the spurious signal in the Y channel vanishes, also completely removes these additional signals within the X channel, i.e., the green curve in Fig. 5(b) only consists of the actual spin signal. Therefore, the offset in the case of $\alpha = \frac{1}{2}$ for $f \rightarrow 0$ Hz must be caused by the other charge-induced artifacts that depend on the common-mode voltage, namely V_L and V_{CMRR} (see Secs. II F and II G). These two signals can appear not only in ac but also dc ($f \rightarrow 0$ Hz) measurements (see the Supplemental Material [44] for a more detailed discussion). The possibility to remove these spurious signals therefore demonstrates that the presented current source is also highly beneficial for dc measurements.

IV. CONCLUSION

We have discussed seven different charge-induced, non-local voltage signals that can appear in a spin measurement, despite the fact that this measurement scheme is repeatedly claimed to be free of such spurious signals. However, it is important to emphasize that the relevance

of each individual charge-induced signal can vary significantly depending on details in device fabrication, properties of the investigated material, device geometry, measurement setup, and measurement technique. In our study, we focused on experimental data that is measured with a lock-in-based technique on graphene spin-valve devices. In such devices we observe that two charge-induced signals normally prevail: the signal that is caused by current spreading (Sec. II A) and the signal that is caused by the capacitor charging currents (Sec. II H). These two signals dominate because tunnel barriers must be used in these devices to overcome the conductivity mismatch problem for an efficient spin injection [69–71]. But it is known that growing homogeneous, pinhole-free tunnel barriers on top of the inert graphene surface is quite challenging without damaging or modifying the underlying graphene [27,100–103]. Pinholes in the tunnel barrier promote the effect of current spreading, whereas strongly varying contact resistances lead to different RC time constants and, therefore, the signal that is caused by the capacitor charging currents. Furthermore, when tunnel barriers are present, a larger bias voltage must be applied to drive the same current as without barriers. Without the possibility to adjust the virtual ground, this unavoidably also increases the common-mode voltage $V_{CM}(t)$ [Fig. 2(b)] and, therefore, all nonlocal charge signals that are driven by $V_{CM}(t)$. In devices without tunnel barriers the relative contribution of each individual charge-induced signal may be completely different.

Nevertheless, the occurrence of all these different charge-induced signals is a general problem, as in the past these artifacts may have been falsely attributed to a variety of spin- or valley-related transport phenomena. For

example, it has already been reported that measurement artifacts have most likely led to erroneous and misleading claims regarding the value of the spin Hall angle in certain materials or the spin-transport properties of topological insulators. Therefore, understanding both the origins of these signals and the specific conditions under which they can appear is crucial for the correct analysis of nonlocal transport experiments, not only in the field of spintronics but also other newly emerging fields such as valleytronics. If available, we have discussed ways how these spurious signals can be minimized. In particular, we demonstrated that our current source, that is able to create a virtual ground in the nonlocal part of the device, can remove any charge-induced signals that are caused by a common-mode voltage.

ACKNOWLEDGMENTS

This project has received funding from the European Union's Horizon 2020 research and innovation programme under Grant Agreement No. 881603 (Graphene Flagship) and the Deutsche Forschungsgemeinschaft (DFG, German Research Foundation) under Germany's Excellence Strategy-Cluster of Excellence Matter and Light for Quantum Computing (ML4Q) EXC 2004/1-390534769, through DFG (BE 2441/9-1 and STA 1146/11-1), and by the Helmholtz Nano Facility (HNF) [104] at the Forschungszentrum Jülich.

-
- [1] I. Žutić, J. Fabian, and S. Das Sarma, Spintronics: Fundamentals and applications, *Rev. Mod. Phys.* **76**, 323 (2004).
- [2] J. Fabian, A. Matos-Abiague, C. Ertler, P. Stano, and I. Žutić, Semiconductor spintronics, *Acta Phys. Slovaca* **57**, 565 (2007).
- [3] M. Johnson and R. H. Silsbee, Coupling of electronic charge and spin at a ferromagnetic-paramagnetic metal interface, *Phys. Rev. B* **37**, 5312 (1988).
- [4] J. Sinova, S. O. Valenzuela, J. Wunderlich, C. H. Back, and T. Jungwirth, Spin Hall effects, *Rev. Mod. Phys.* **87**, 1213 (2015).
- [5] A. Hirohata, K. Yamada, Y. Nakatani, I.-L. Prejbeanu, B. Diény, P. Pirro, and B. Hillebrands, Review on spintronics: Principles and device applications, *J. Magn. Magn. Mater.* **509**, 166711 (2020).
- [6] S. Roche, J. Åkerman, B. Beschoten, J.-C. Charlier, M. Chshiev, S. P. Dash, B. Dlubak, J. Fabian, A. Fert, M. Guimarães, F. Guinea, I. Grigorieva, C. Schönberger, P. Seneor, C. Stampfer, S. O. Valenzuela, X. Waintal, and B. van Wees, Graphene spintronics: The European flagship perspective, *2D Mater.* **2**, 030202 (2015).
- [7] A. Avsar, H. Ochoa, F. Guinea, B. Özyilmaz, B. J. van Wees, and I. J. Vera-Marun, Colloquium: Spintronics in graphene and other two-dimensional materials, *Rev. Mod. Phys.* **92**, 021003 (2020).
- [8] J. F. Sierra, J. Fabian, R. K. Kawakami, S. Roche, and S. O. Valenzuela, Van der Waals heterostructures for spintronics and opto-spintronics, *Nat. Nanotechnol.* **16**, 856 (2021).
- [9] R. V. Gorbachev R., J. C. W. Song, G. L. Yu, A. V. Kretinin, F. Withers, Y. Cao, A. Mishchenko, I. V. Grigorieva, K. S. Novoselov, L. S. Levitov, and A. K. Geim, Detecting topological currents in graphene superlattices, *Science* **346**, 448 (2014).
- [10] M. Sui, G. Chen, L. Ma, W.-Y. Shan, D. Tian, K. Watanabe, T. Taniguchi, X. Jin, W. Yao, D. Xiao, and Y. Zhang, Gate-tunable topological valley transport in bilayer graphene, *Nat. Phys.* **11**, 1027 (2015).
- [11] Y. Shimazaki, M. Yamamoto, I. V. Borzenets, K. Watanabe, T. Taniguchi, and S. Tarucha, Generation and detection of pure valley current by electrically induced Berry curvature in bilayer graphene, *Nat. Phys.* **11**, 1032 (2015).
- [12] K. Endo, K. Komatsu, T. Iwasaki, E. Watanabe, D. Tsuya, K. Watanabe, T. Taniguchi, Y. Noguchi, Y. Wakayama, Y. Morita, and S. Moriyama, Topological valley currents in bilayer graphene/hexagonal boron nitride superlattices, *Appl. Phys. Lett.* **114**, 243105 (2019).
- [13] M. Ribeiro, S. R. Power, S. Roche, L. E. Hueso, and F. Casanova, Scale-invariant large nonlocality in polycrystalline graphene, *Nat. Commun.* **8**, 2198 (2017).
- [14] J. M. Marmolejo-Tejada, J. H. García, M. D. Petrović, P.-H. Chang, X.-L. Sheng, A. Cresti, P. Plecháč, S. Roche, and B. K. Nikolić, Deciphering the origin of nonlocal resistance in multiterminal graphene on hexagonal-boron-nitride with ab initio quantum transport: Fermi surface edge currents rather than Fermi sea topological valley currents, *J. Phys.: Mater.* **1**, 015006 (2018).
- [15] A. Aharon-Steinberg, A. Marguerite, D. J. Perello, K. Bagani, T. Holder, Y. Myasoedov, L. S. Levitov, A. K. Geim, and E. Zeldov, Long-range nontopological edge currents in charge-neutral graphene, *Nature* **593**, 528 (2021).
- [16] L. Foa-Torres and S. Valenzuela, A valley of opportunities, *Phys. World* **34**, 43 (2021).
- [17] S. Roche, S. R. Power, B. K. Nikolić, J. H. García, and A.-P. Jauho, Have mysterious topological valley currents been observed in graphene superlattices?, *J. Phys.: Mater.* **5**, 021001 (2022).
- [18] G. Mihajlović, J. E. Pearson, M. A. Garcia, S. D. Bader, and A. Hoffmann, Negative Nonlocal Resistance in Mesoscopic Gold Hall Bars: Absence of the Giant Spin Hall Effect, *Phys. Rev. Lett.* **103**, 166601 (2009).
- [19] T. Völkl, D. Kochan, T. Ebnet, S. Ringer, D. Schiermeier, P. Nagler, T. Korn, C. Schüller, J. Fabian, D. Weiss, and J. Eroms, Absence of a giant spin Hall effect in plasma-hydrogenated graphene, *Phys. Rev. B* **99**, 085401 (2019).
- [20] A. A. Kaverzin and B. J. van Wees, Electron transport nonlocality in monolayer graphene modified with hydrogen silsesquioxane polymerization, *Phys. Rev. B* **91**, 165412 (2015).
- [21] D. Van Tuan, J. M. Marmolejo-Tejada, X. Waintal, B. K. Nikolić, S. O. Valenzuela, and S. Roche, Spin Hall Effect and Origins of Nonlocal Resistance in Adatom-Decorated Graphene, *Phys. Rev. Lett.* **117**, 176602 (2016).

- [22] Y. Wang, X. Cai, J. Reutt-Robey, and M. S. Fuhrer, Neutral-current Hall effects in disordered graphene, *Phys. Rev. B* **92**, 161411 (2015).
- [23] E. K. de Vries, A. M. Kamerbeek, N. Koirala, M. Brahlek, M. Salehi, S. Oh, B. J. van Wees, and T. Banerjee, Towards the understanding of the origin of charge-current-induced spin voltage signals in the topological insulator Bi_2Se_3 , *Phys. Rev. B* **92**, 201102 (2015).
- [24] M. V. Kamalakar, C. Groenvelde, A. Dankert, and S. P. Dash, Long distance spin communication in chemical vapour deposited graphene, *Nat. Commun.* **6**, 6766 (2015).
- [25] W. Yan, O. Txoperena, R. Llopis, H. Dery, L. E. Hueso, and F. Casanova, A two-dimensional spin field-effect switch, *Nat. Commun.* **7**, 13372 (2016).
- [26] J. Xu, T. Zhu, Y. K. Luo, Y.-M. Lu, and R. K. Kawakami, Strong and Tunable Spin-Lifetime Anisotropy in Dual-Gated Bilayer Graphene, *Phys. Rev. Lett.* **121**, 127703 (2018).
- [27] M. Cubukcu, M.-B. Martin, P. Laczkowski, C. Vergnaud, A. Marty, J.-P. Attané, P. Seneor, A. Anane, C. Deranlot, A. Fert, S. Auffret, C. Ducruet, L. Notin, L. Vila, and M. Jamet, Ferromagnetic tunnel contacts to graphene: Contact resistance and spin signal, *J. Appl. Phys.* **117**, 083909 (2015).
- [28] T. S. Ghiasi, A. A. Kaverzin, P. J. Blah, and B. J. van Wees, Charge-to-spin conversion by the Rashba-Edelstein effect in two-dimensional van der Waals heterostructures up to room temperature, *Nano Lett.* **19**, 5959 (2019).
- [29] W. Amamou, G. Stecklein, S. J. Koester, P. A. Crowell, and R. K. Kawakami, Spin Absorption by In Situ Deposited Nanoscale Magnets on Graphene Spin Valves, *Phys. Rev. Appl.* **10**, 044050 (2018).
- [30] S. Ringer, M. Rosenauer, T. Völkl, M. Kadur, F. Hopperdietzel, D. Weiss, and J. Eroms, Spin field-effect transistor action via tunable polarization of the spin injection in a Co/MgO/graphene contact, *Appl. Phys. Lett.* **113**, 132403 (2018).
- [31] T. Zhu, S. Singh, J. Katoch, H. Wen, K. Belashchenko, I. Žutić, and R. K. Kawakami, Probing tunneling spin injection into graphene via bias dependence, *Phys. Rev. B* **98**, 054412 (2018).
- [32] Z. M. Gebeyehu, S. Parui, J. F. Sierra, M. Timmermans, M. J. Esplandiú, S. Brems, C. Huyghebaert, K. Garello, M. V. Costache, and S. O. Valenzuela, Spin communication over 30 μm long channels of chemical vapor deposited graphene on SiO_2 , *2D Mater.* **6**, 034003 (2019).
- [33] C. K. Safeer, J. Ingla-Aynés, F. Herling, J. H. Garcia, M. Vila, N. Ontoso, M. R. Calvo, S. Roche, L. E. Hueso, and F. Casanova, Room-temperature spin Hall effect in graphene/ MoS_2 van der Waals heterostructures, *Nano Lett.* **19**, 1074 (2019).
- [34] B. Zhao, D. Khokhriakov, B. Karpiak, A. M. Hoque, L. Xu, L. Shen, Y. P. Feng, X. Xu, Y. Jiang, and S. P. Dash, Electrically controlled spin-switch and evolution of Hanle spin precession in graphene, *2D Mater.* **6**, 035042 (2019).
- [35] Y. Liu, C. Zeng, J. Ding, J. Zhong, Y. Gao, X. Kuang, J. Yu, L. Cao, J. He, and Z. Liu, Effect of the low-resistance tunnel barriers induced inhomogeneous spin current distribution in graphene crossed configuration lateral spin valve, *AIP Adv.* **9**, 115005 (2019).
- [36] M. Drögeler, C. Franzen, F. Volmer, T. Pohlmann, L. Banszerus, M. Wolter, K. Watanabe, T. Taniguchi, C. Stampfer, and B. Beschoten, Spin lifetimes exceeding 12 ns in graphene nonlocal spin valve devices, *Nano Lett.* **16**, 3533 (2016).
- [37] F. Volmer, M. Drögeler, E. Maynicke, N. von den Driesch, M. L. Boschen, G. Güntherodt, C. Stampfer, and B. Beschoten, Suppression of contact-induced spin dephasing in graphene/MgO/Co spin-valve devices by successive oxygen treatments, *Phys. Rev. B* **90**, 165403 (2014).
- [38] L. A. Benítez, W. Saverio Torres, J. F. Sierra, M. Timmermans, J. H. Garcia, S. Roche, M. V. Costache, and S. O. Valenzuela, Tunable room-temperature spin galvanic and spin Hall effects in van der Waals heterostructures, *Nat. Mater.* **19**, 170 (2020).
- [39] J. Panda, M. Ramu, O. Karis, T. Sarkar, and M. V. Kamalakar, Ultimate spin currents in commercial chemical vapor deposited graphene, *ACS Nano* **14**, 12771 (2020).
- [40] S. Ringer, S. Hartl, M. Rosenauer, T. Völkl, M. Kadur, F. Hopperdietzel, D. Weiss, and J. Eroms, Measuring anisotropic spin relaxation in graphene, *Phys. Rev. B* **97**, 205439 (2018).
- [41] M. Brands and G. Dumpich, Experimental determination of anisotropy and demagnetizing factors of single Co nanowires by magnetoresistance measurements, *J. Appl. Phys.* **98**, 014309 (2005).
- [42] B. Leven and G. Dumpich, Resistance behavior and magnetization reversal analysis of individual Co nanowires, *Phys. Rev. B* **71**, 064411 (2005).
- [43] F. Volmer, M. Drögeler, T. Pohlmann, G. Güntherodt, C. Stampfer, and B. Beschoten, Contact-induced charge contributions to non-local spin transport measurements in Co/MgO/graphene devices, *2D Mater.* **2**, 024001 (2015).
- [44] See Supplemental Material at <http://link.aps.org/supplemental/10.1103/PhysRevApplied.18.014028> for (1) a discussion of all technical aspects of the voltage-controlled current source with all information necessary to rebuild the electronics, (2) measurements about its accuracy, bandwidth, and stability during fast transients, (3) a discussion and measurements of how a common-mode voltage can even impact local measurements, (4) practical hints on how to adjust the virtual ground, (5) a discussion about applications and limitations of the current source, and (6) some practical advice both on the use of the current source and on the investigation of the charge-induced signals in nonlocal measurements.
- [45] M. Johnson and R. H. Silsbee, Calculation of nonlocal baseline resistance in a quasi-one-dimensional wire, *Phys. Rev. B* **76**, 153107 (2007).
- [46] J. Hu, G. Stecklein, D. A. Deen, Q. Su, P. A. Crowell, and S. J. Koester, Scaling of the nonlocal spin and baseline resistances in graphene lateral spin valves, *IEEE Trans. Electron Devices* **66**, 5003 (2019).
- [47] D. Ruffer, F. D. Czeschka, R. Gross, and S. T. B. Goennenwein, Experimental observation of an enhanced

- anisotropic magnetoresistance in non-local configuration, *Appl. Phys. Lett.* **99**, 142112 (2011).
- [48] C. K. Safeer, F. Herling, W. Y. Choi, N. Ontoso, J. Ingla-Aynés, L. E. Hueso, and F. Casanova, Reliability of spin-to-charge conversion measurements in graphene-based lateral spin valves, *2D Mater.* **9**, 015024 (2021).
- [49] J. Renard, M. Studer, and J. A. Folk, Origins of Nonlocality Near the Neutrality Point in Graphene, *Phys. Rev. Lett.* **112**, 116601 (2014).
- [50] F. L. Bakker, A. Slachter, J.-P. Adam, and B. J. van Wees, Interplay of Peltier and Seebeck Effects in Nanoscale Non-local Spin Valves, *Phys. Rev. Lett.* **105**, 136601 (2010).
- [51] K. S. Das, F. K. Dejene, B. J. van Wees, and I. J. Vera-Marun, Anisotropic Hanle line shape via magnetothermoelectric phenomena, *Phys. Rev. B* **94**, 180403 (2016).
- [52] K. Gopinadhan, Y. J. Shin, R. Jalil, T. Venkatesan, A. K. Geim, A. H. C. Neto, and H. Yang, Extremely large magnetoresistance in few-layer graphene/boron-nitride heterostructures, *Nat. Commun.* **6**, 8337 (2015).
- [53] S. Hu and T. Kimura, Anomalous Nernst-Ettingshausen effect in nonlocal spin valve measurement under high-bias current injection, *Phys. Rev. B* **87**, 014424 (2013).
- [54] R. K. Bennet, A. Hojem, and B. L. Zink, Thermal gradients and anomalous Nernst effects in membrane-supported nonlocal spin valves, *Phys. Rev. B* **100**, 104404 (2019).
- [55] T. Ariki, T. Nomura, K. Ohnishi, and T. Kimura, Effective suppression of thermoelectric voltage in nonlocal spin-valve measurement, *Appl. Phys. Express* **10**, 063004 (2017).
- [56] N. Yang, X. Xu, G. Zhang, and B. Li, Thermal transport in nanostructures, *AIP Adv.* **2**, 041410 (2012).
- [57] A. A. Balandin, Thermal properties of graphene and nanostructured carbon materials, *Nat. Mater.* **10**, 569 (2011).
- [58] Y. M. Zuev, W. Chang, and P. Kim, Thermoelectric and Magnetothermoelectric Transport Measurements of Graphene, *Phys. Rev. Lett.* **102**, 096807 (2009).
- [59] A. Harzheim, C. Evangeli, O. V. Kolosov, and P. Gehring, Direct mapping of local Seebeck coefficient in 2D material nanostructures via scanning thermal gate microscopy, *2D Mater.* **7**, 041004 (2020).
- [60] P. R. Gray, P. J. Hurst, S. H. Lewis, and R. G. Meyer, *Analysis and Design of Analog Integrated Circuits* (John Wiley & Sons, Inc., Hoboken, NJ, USA, 2009).
- [61] P. R. Gray and R. G. Meyer, MOS operational amplifier design—a tutorial overview, *IEEE J. Solid-State Circuits* **17**, 969 (1982).
- [62] P. R. Kinget, Device mismatch and tradeoffs in the design of analog circuits, *IEEE J. Solid-State Circuits* **40**, 1212 (2005).
- [63] P. Märki, B. A. Braem, and T. Ihn, Temperature-stabilized differential amplifier for low-noise DC measurements, *Rev. Sci. Instrum.* **88**, 085106 (2017).
- [64] J. Ekin, *Experimental Techniques for Low-Temperature Measurements: Cryostat Design, Material Properties and Superconductor Critical-Current Testing* (Oxford University Press Inc., New York, 2010).
- [65] F. Fiori and P. S. Crovetto, Nonlinear effects of radio-frequency interference in operational amplifiers, *IEEE Trans. Circuits Syst. I: Fundam. Theory Appl.* **49**, 367 (2002).
- [66] A. Poulton, Effect of conducted EMI on the DC performance of operational amplifiers, *Electron. Lett.* **30**, 282 (1994).
- [67] J.-M. Redouté and M. Steyaert, Measurement of EMI induced input offset voltage of an operational amplifier, *Electron. Lett.* **43**, 1088 (2007).
- [68] A. De Sanctis, J. D. Meheew, S. Alkhalifa, C. P. Tate, A. White, A. R. Woodgate, M. F. Craciun, and S. Russo, Novel circuit design for high-impedance and non-local electrical measurements of two-dimensional materials, *Rev. Sci. Instrum.* **89**, 024705 (2018).
- [69] E. I. Rashba, Theory of electrical spin injection: Tunnel contacts as a solution of the conductivity mismatch problem, *Phys. Rev. B* **62**, R16267 (2000).
- [70] G. Schmidt, D. Ferrand, L. W. Molenkamp, A. T. Filip, and B. J. van Wees, Fundamental obstacle for electrical spin injection from a ferromagnetic metal into a diffusive semiconductor, *Phys. Rev. B* **62**, R4790 (2000).
- [71] A. Fert and H. Jaffrès, Conditions for efficient spin injection from a ferromagnetic metal into a semiconductor, *Phys. Rev. B* **64**, 184420 (2001).
- [72] J. Szynowski, CMRR analysis of instrumentation amplifiers, *Electron. Lett.* **19**, 547 (1983).
- [73] R. Pallas-Areny and J. G. Webster, Common mode rejection ratio in differential amplifiers, *IEEE Trans. Instrum. Meas.* **40**, 669 (1991).
- [74] S. Wang and F. C. Lee, Investigation of the transformation between differential-mode and common-mode noises in an EMI filter due to unbalance, *IEEE Trans. Electromagn. Compat.* **52**, 578 (2010).
- [75] H. W. Ott, *Electromagnetic Compatibility Engineering* (John Wiley & Sons, Inc., Hoboken, NJ, USA, 2009).
- [76] The data supporting the findings of this study are available in a Zenodo repository under [doi:10.5281/zenodo.6525020](https://doi.org/10.5281/zenodo.6525020). There we provide (1) all data presented in each figure, (2) the LTspice models for each simulation, (3) Gerber files of the printed circuit board used for our current source, (4) the corresponding Altium Designer files, and (5) a bill of materials.
- [77] B. Karpiak, A. Dankert, A. W. Cummings, S. R. Power, S. Roche, and S. P. Dash, 1D ferromagnetic edge contacts to 2D graphene/h-BN heterostructures, *2D Mater.* **5**, 014001 (2017).
- [78] I. Groen, V. T. Pham, N. Leo, A. Marty, L. E. Hueso, and F. Casanova, Disentangling Spin, Anomalous, and Planar Hall Effects in Ferromagnet-Heavy-Metal Nanostructures, *Phys. Rev. Appl.* **15**, 044010 (2021).
- [79] O. Txoperena and F. Casanova, Spin injection and local magnetoresistance effects in three-terminal devices, *J. Phys. D: Appl. Phys.* **49**, 133001 (2016).
- [80] S. P. Dash, S. Sharma, J. C. Le Breton, J. Peiro, H. Jaffrès, J.-M. George, A. Lemaître, and R. Jansen, Spin precession and inverted Hanle effect in a semiconductor near a finite-roughness ferromagnetic interface, *Phys. Rev. B* **84**, 054410 (2011).

- [81] P. K. Muduli, J. Barzola-Quiquia, S. Dusari, A. Ballestar, F. Bern, W. Böhlmann, and P. Esquinazi, Large local Hall effect in pin-hole dominated multigraphene spin-valves, *Nanotechnology* **24**, 015703 (2012).
- [82] A. J. Berger, M. R. Page, H. Wen, K. M. McCreary, V. P. Bhallamudi, R. K. Kawakami, and P. Chris Hammel, Correlating spin transport and electrode magnetization in a graphene spin valve: Simultaneous magnetic microscopy and non-local measurements, *Appl. Phys. Lett.* **107**, 142406 (2015).
- [83] L. Li, J. Zhang, G. Myeong, W. Shin, H. Lim, B. Kim, S. Kim, T. Jin, S. Cavill, B. S. Kim, C. Kim, J. Lischner, A. Ferreira, and S. Cho, Gate-tunable reversible Rashba-Edelstein effect in a few-layer graphene/2H-TaS₂ heterostructure at room temperature, *ACS Nano* **14**, 5251 (2020).
- [84] M. Z. Hasan and C. L. Kane, Colloquium: Topological insulators, *Rev. Mod. Phys.* **82**, 3045 (2010).
- [85] C. H. Li, O. M. J. van't Erve, J. T. Robinson, Y. Liu, L. Li, and B. T. Jonker, Electrical detection of charge-current-induced spin polarization due to spin-momentum locking in Bi₂Se₃, *Nat. Nanotechnol.* **9**, 218 (2014).
- [86] J. Tang, L.-T. Chang, X. Kou, K. Murata, E. S. Choi, M. Lang, Y. Fan, Y. Jiang, M. Montazeri, W. Jiang, Y. Wang, L. He, and K. L. Wang, Electrical detection of spin-polarized surface states conduction in (Bi_{0.53}Sb_{0.47})₂Te₃ topological insulator, *Nano Lett.* **14**, 5423 (2014).
- [87] Y. Ando, T. Hamasaki, T. Kurokawa, K. Ichiba, F. Yang, M. Novak, S. Sasaki, K. Segawa, Y. Ando, and M. Shiraishi, Electrical detection of the spin polarization due to charge flow in the surface state of the topological insulator Bi_{1.5}Sb_{0.5}Te_{1.7}Se_{1.3}, *Nano Lett.* **14**, 6226 (2014).
- [88] A. Dankert, J. Geurs, M. V. Kamalakar, S. Charpentier, and S. P. Dash, Room temperature electrical detection of spin polarized currents in topological insulators, *Nano Lett.* **15**, 7976 (2015).
- [89] J. Tian, I. Miotkowski, S. Hong, and Y. P. Chen, Electrical injection and detection of spin-polarized currents in topological insulator Bi₂Te₂Se, *Sci. Rep.* **5**, 14293 (2015).
- [90] J. S. Lee, A. Richardella, D. R. Hickey, K. A. Mkhoyan, and N. Samarth, Mapping the chemical potential dependence of current-induced spin polarization in a topological insulator, *Phys. Rev. B* **92**, 155312 (2015).
- [91] F. Yang, S. Ghatak, A. A. Taskin, K. Segawa, Y. Ando, M. Shiraishi, Y. Kanai, K. Matsumoto, A. Rosch, and Y. Ando, Switching of charge-current-induced spin polarization in the topological insulator BiSbTeSe₂, *Phys. Rev. B* **94**, 075304 (2016).
- [92] T. Seki, Y. Hasegawa, S. Mitani, S. Takahashi, H. Imaura, S. Maekawa, J. Nitta, and K. Takanashi, Giant spin Hall effect in perpendicularly spin-polarized FePt/Au devices, *Nat. Mater.* **7**, 125 (2008).
- [93] J. Balakrishnan, G. Kok Wai Koon, M. Jaiswal, A. H. Castro Neto, and B. Özyilmaz, Colossal enhancement of spin-orbit coupling in weakly hydrogenated graphene, *Nat. Phys.* **9**, 284 (2013).
- [94] J. Balakrishnan, G. K. W. Koon, A. Avsar, Y. Ho, J. H. Lee, M. Jaiswal, S.-J. Baeck, J.-H. Ahn, A. Ferreira, M. A. Cazalilla, A. H. C. Neto, and B. Özyilmaz, Giant spin Hall effect in graphene grown by chemical vapour deposition, *Nat. Commun.* **5**, 4748 (2014).
- [95] M. Drögeler, F. Volmer, M. Wolter, B. Terrés, K. Watanabe, T. Taniguchi, G. Güntherodt, C. Stampfer, and B. Beschoten, Nanosecond spin lifetimes in single- and few-layer graphene-hBN heterostructures at room temperature, *Nano Lett.* **14**, 6050 (2014).
- [96] F. Volmer, I. Seidler, T. Bisswanger, J.-S. Tu, L. R. Schreiber, C. Stampfer, and B. Beschoten, How to solve problems in micro- and nanofabrication caused by the emission of electrons and charged metal atoms during e-beam evaporation, *J. Phys. D: Appl. Phys.* **54**, 225304 (2021).
- [97] M. Drögeler, L. Banszerus, F. Volmer, T. Taniguchi, K. Watanabe, B. Beschoten, and C. Stampfer, Dry-transferred CVD graphene for inverted spin valve devices, *Appl. Phys. Lett.* **111**, 152402 (2017).
- [98] M. Drögeler, F. Volmer, M. Wolter, K. Watanabe, T. Taniguchi, D. Neumaier, C. Stampfer, and B. Beschoten, Nanosecond spin lifetimes in bottom-up fabricated bilayer graphene spin-valves with atomic layer deposited AlO spin injection and detection barriers, *Phys. Status Solidi (b)* **252**, 2395 (2015).
- [99] T. Bisswanger, Z. Winter, A. Schmidt, F. Volmer, K. Watanabe, T. Taniguchi, C. Stampfer, and B. Beschoten, CVD bilayer graphene spin valves with 26 μm spin diffusion length at room temperature, *Nano Lett.* **22**, 4949 (2022).
- [100] B. Canto, C. P. Gouvea, B. S. Archanjo, J. E. Schmidt, and D. L. Baptista, On the structural and chemical characteristics of Co/Al₂O₃/graphene interfaces for graphene spintronic devices, *Sci. Rep.* **5**, 14332 (2015).
- [101] R. H. J. Vervuurt, W. M. M. E. Kessels, and A. A. Bol, Atomic layer deposition for graphene device integration, *Adv. Mater. Interfaces* **4**, 1700232 (2017).
- [102] A. L. Hsu, R. J. Koch, M. T. Ong, W. Fang, M. Hofmann, K. K. Kim, T. Seyller, M. S. Dresselhaus, E. J. Reed, J. Kong, and T. Palacios, Surface-induced hybridization between graphene and titanium, *ACS Nano* **8**, 7704 (2014).
- [103] P. Ahlberg, F. O. L. Johansson, Z.-B. Zhang, U. Jansson, S.-L. Zhang, A. Lindblad, and T. Nyberg, Defect formation in graphene during low-energy ion bombardment, *APL Mater.* **4**, 046104 (2016).
- [104] Research Center Jülich GmbH, HNF—Helmholtz nano facility, *J. Large Scale Res. Facil.* **3**, A112 (2017).